Applied Clay Science 206 (2021) 106075

Contents lists available at ScienceDirect

Applied Clay Science

journal homepage: www.elsevier.com/locate/clay

Research Paper

A density functional theory (DFT) investigation of how small molecules and atmospheric pollutants relevant to art conservation adsorb on kaolinite

Jessica E. Heimann, Ryan T. Grimes, Zeev Rosenzweig, Joseph W. Bennett *

Department of Chemistry and Biochemistry, University of Maryland Baltimore County, Baltimore, MD 21250, USA

ARTICLE INFO

Keywords:
Density functional theory (DFT)
Kaolinite
Hydrogen bonding
Adsorption
Small molecule
Cultural heritage

ABSTRACT

The physio-chemical properties of the clay mineral kaolinite – the main component of porcelain – play a vital role in understanding how a porcelain object interacts with its environment. Understanding these interactions is imperative for the development of non-destructive yet effective conservation methods to preserve, treat, and restore porcelain objects of cultural heritage importance. To gain insight into the surface properties and behavior of kaolinite across a wide range of environments, we use density functional theory (DFT) to probe how a representative set of small molecules and atmospheric pollutants interact with a native kaolinite (001) surface, both in vacuum and with explicit hydration. By investigating selected atmospheric pollutants, acids, and sodium salts under different conditions, we identify the scenarios that are most disruptive to the native kaolinite surface. Specifically, we demonstrate that protic acids and sodium salts generally interact with the surface more strongly than common small molecule pollutants. Our results also indicate that adsorbates containing a central sulfur atom with a positive oxidation state are particularly deleterious to the kaolinite surface. Furthermore, to explore the interactions between a fired or partially fired porcelain object and relevant chemicals, we also model a partially dehydrated kaolinite surface and probe its interactions with three selected adsorbates. The trends elucidated throughout this study allow us to suggest a series of guidelines for the care of porcelain objects.

1. Introduction

Kaolinite [$Al_2Si_2O_5(OH)_4$] is an aluminosilicate clay mineral formed from repeating layers of one silica sheet, with each silicon atom tetrahedrally coordinated to four oxygen atoms, and one gibbsite-type sheet, with each aluminum atom octahedrally coordinated to four hydroxyl groups and two oxygen atoms (Sposito et al., 1999; Brigatti et al., 2011). The hydroxylated (001) surface of the gibbsite layer and the siloxane (00−1) surface of each adjacent layer are linked via interlayer hydrogen bonds (Tosoni et al., 2006; Hu and Michaelides, 2010). Almost no substitution occurs within the structural lattice of kaolinite, which results in minimal charge across each layer and a low cation-exchange capacity (Murray, 2000; Bhattacharyya and Gupta, 2008). Kaolinite also has a low shrink-swell capacity and is relatively insoluble (Sposito, 2008), additional characteristics that make this clay mineral useful in many applications. As a result of these unique physical and chemical properties, kaolinite has been used in a wide range of industries including paper, paint, catalysis, plastics, and ceramics. Although the largest use of kaolinite is now in paper coating, the first sophisticated technological use of this clay mineral was in porcelain objects over two thousand years ago in Jingdezhen, China (Murray, 2000, 2006; Schroeder and Erickson, 2014). As the main component of porcelain, kaolinite has since remained a foundational material within the ceramics industry and other disciplines in the field of cultural heritage (Carty and Senapati, 1998).

In order to properly handle or restore a porcelain object in a non-destructive yet effective manner, it is imperative to understand how a kaolinite surface interacts with molecules to which it may be exposed. These include atmospheric pollutants, cleaning agents, acids, and salts. The adsorption of different ions and molecules on a kaolinite surface has been explored in numerous studies, using both experimental (Zachara et al., 1988; Torn et al., 2003; Angelini et al., 2007; Li and Gallus, 2007; Bhattacharyya and Gupta, 2008; Li et al., 2010; Rubasinghege et al., 2013; Zhang et al., 2014; Chen and Lu, 2015; Alstadt et al., 2016; Alshameri et al., 2018) and computational (Kremleva et al., 2008; Martorell et al., 2010; He et al., 2013; Lee et al., 2013; Song et al., 2013; Zhao and He, 2014; Wang et al., 2015; Han et al., 2016; Chen et al., 2017; Wang et al., 2017; Wang et al., 2018; Chen et al., 2019; Liu et al.,

* Corresponding author.
E-mail address: bennettj@umbc.edu (J.W. Bennett).

https://doi.org/10.1016/j.clay.2021.106075
Received 17 November 2020; Received in revised form 22 March 2021; Accepted 24 March 2021

2019) techniques. These studies, however, primarily consider adsorption scenarios on kaolinite that relate to mineral processing, cement/concrete or paper manufacturing, toxic heavy metal removal and water treatment, or environmental and geological processes. To our knowledge, there has been no work systematically exploring how common atmospheric pollutants, acids, sodium salts, and other adsorbent molecules relevant to art conservation could perturb an exposed kaolinite surface. To probe these adsorption events on an atomistic level and provide insight that will potentially facilitate the conservation and preservation of kaolinite-based ceramics, we turn to density functional theory (DFT), a quantum mechanical method capable of examining how atoms and molecules interact with mineral surfaces (Jones, 2015; Jain et al., 2016; Bennett et al., 2019).

In the last 15 years, DFT has become an invaluable tool in both modeling the structure and dynamics of layered materials (Heinz and Suter, 2004; Heinz, 2006; Cygan et al., 2009) and delineating mineral surface structure-property relationships, specifically atomistic adsorption interactions important to geochemistry (Kubicki et al., 2007; Kubicki et al., 2009; Mason et al., 2015). Detailed studies have been published on the mechanisms of mineral surface adsorption reactions concerning rutile (Zhang et al., 2004; Zhang et al., 2006), hematite (Corum et al., 2017; Bennett et al., 2019), alumina (Mason et al., 2011; Corum et al., 2018), and aluminum nanoclusters (Bennett et al., 2017; Bjorklund et al., 2019). In practice, these calculations are performed in vacuum or using implicit solvation to mimic aqueous conditions in order to guide experimental investigations into surface reactivity. DFT modeling efforts usually start by matching the properties of published bulk crystal structures. From there, the bulk structure is used to create a supercell slab of variable repeat dimensions, which is then cleaved along a given direction to create a surface. For example, hematite, alumina and delafossite structures can be easily cleaved along the c-axis to reveal the (001) set of planes (Corum et al., 2017; Huang et al., 2017). Once these surfaces are exposed, DFT simulations can be used to change surface terminations and add adsorbates in outer- or innersphere coordination (of variable orientations) to determine environmental reactivity (Mason et al., 2015). With advances in computer architectures, it has also become common to create comparative studies of adsorption to and/or release of contaminants from minerals common to soils such as Pb, H_xAsO_4, and H_xPO_4 (Mason et al., 2009; Goffinet and Mason, 2012; Tamijani et al., 2020), in an effort to inform remediation and treatment efforts.

In this work, we use DFT to explore how a representative set of small molecules interact with a kaolinite surface, both in vacuum and with explicit hydration. Specifically, we investigate a range of atmospheric pollutants, acids, and sodium salts to identify which sets of conditions are most disruptive to the native kaolinite surface. The detailed atomistic information obtained from DFT allows us to delineate adsorption reactivity trends for a wide variety of chemical environments and create a set of guidelines for the care of unfired porcelain objects of cultural heritage significance. Furthermore, to better understand the interactions between a fired or partially fired porcelain object and possible pollutants, we model a partially dehydrated kaolinite surface and probe its interactions with three selected adsorbates.

2. Computational details

All calculations described here employ periodic DFT methods (Hohenberg and Kohn, 1964; Kohn and Sham, 1965) and are carried out using Quantum Espresso, an open source software package (Giannozzi et al., 2009; Giannozzi et al., 2017). All atoms are represented using GBRV-type ultrasoft pseudopotentials (Vanderbilt, 1990; Garrity et al., 2014). A plane-wave cutoff of 40 Ry and charge density cutoff of 320 Ry are employed for all calculations, in line with similar surface studies (Bennett et al., 2018a; Bennett et al., 2018b; Bennett et al., 2020). Bulk structural relaxations use a 6x6x6 k-point grid (Monkhorst and Pack, 1976), and the convergence criteria for self-consistent relaxations is 5×10^{-6} eV. The results from the bulk relaxations are then used to create a 2x1x1 supercell with vacuum in the c-direction. The k-point sampling for all surface and surface-adsorbate calculations is 3x6x1. Geometry optimization of all surface-adsorbate interactions did not include fixing any layers, as detailed in Corum et al. (2017) where all atoms are free to relax. All calculations are performed at the GGA level using the Wu-Cohen (WC) modified PBE-GGA exchange correlation functional for solids (Perdew et al., 1996; Wu and Cohen, 2006). Results from our survey of exchange-correlation tests are included in the Supplemental Materials (Table S1).

3. Results and discussion

3.1. Bulk kaolinite

The triclinic structure of bulk kaolinite (Figs. 1 and 2a) has been well characterized by experimental techniques such as neutron and X-ray powder diffraction (Young and Hewat, 1988; Bish, 1993) as well as numerous computational simulations (Sato et al., 2004; Tosoni et al., 2006; Hu and Michaelides, 2008; Lee et al., 2013). The primitive bulk cell contains 34 atoms and is assigned to the triclinic P1 space group. Tables 1 and 2 provide the lattice parameters and selected interatomic bond distances for the kaolinite unit cell optimized in this work, respectively, and compares them to the previously reported experimental and computational values. As shown in Tables 1 and 2, the lattice constants and bond lengths obtained here are in good agreement with those reported. The largest deviation from the experimental parameters reported in Young and Hewat (1988) is in the lattice constant b, as our methodology overestimates this parameter by 0.62%. The value determined in this work, however, closely matches the computational values previously reported. In fact, the deviations from experimental lattice parameters observed here generally mirror the trends reported in previous computational studies. For example, an overestimation of a and b and an underestimation of α and γ were also reported in Tunega et al. (2012) (Table 1, Entry 3), Weck et al. (2015) (Table 1, Entry 4), and Richard and Rendtorff (2019) (Table 1, Entry 6). The data listed in Table 1 emphasizes that DFT performed at the basic PBE-GGA level (Table 1, Entry 4) overestimates the lattice parameters more than dispersion-corrected DFT (Table 1, Entry 5) or DFT performed at the PBEsol or WC modified PBE-GGA level (Table 1, Entries 3 and 6–7), even though DFT-D2 and PBEsol/WC modified PBE-GGA are parametrized for molecules and solids, respectively. Specifically, the PBE-GGA functional

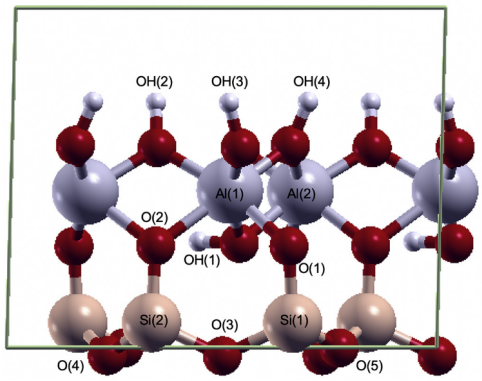

Fig. 1. The structure of kaolinite, as viewed along the a-axis. Atom labels correspond to Table 2. Aluminum, silicon, oxygen, and hydrogen are shown in gray, peach, red, and white, respectively. The unit cell is shown in green.

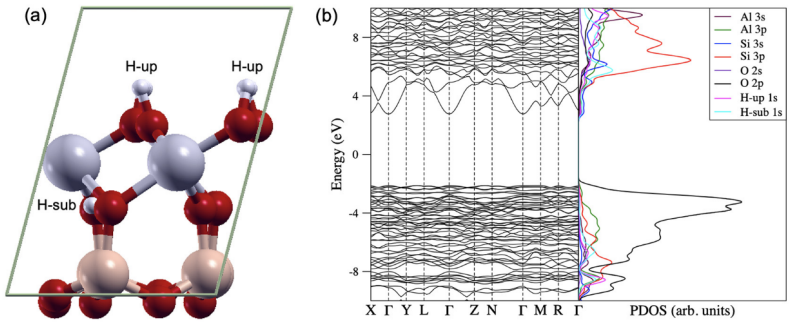

Fig. 2. (a) Bulk kaolinite, as viewed along the b-axis. (b) The electronic band structure (left) and PDOS (right) of bulk kaolinite. A direct bandgap of 4.87 eV was computed at the Γ point. The occupied states are composed primarily of O 2p orbitals (black line in PDOS), and the unoccupied states are composed mostly of the cation states (Si, Al, and H). Distinct electronic structures corresponding to the surface H (H-up) and the subsurface H (H-sub) are present in the PDOS.

Table 1
Lattice parameters for the triclinic unit cell of kaolinite.

Entry	Reference	a (Å)	b (Å)	c (Å)	α (°)	β (°)	γ (°)
1	Young and Hewat, 1988[a]	5.1497(1)	8.9350(7)	7.3854(9)	91.9283(4)	105.0439(4)	89.7921(5)
2	Bish, 1993[b]	5.1535(3)	8.9419(5)	7.3906(4)	91.926(2)	105.046(2)	89.797(2)
3	Tunega et al., 2012[c]	5.166	8.970	7.306	91.82	104.99	89.78
4	Weck et al., 2015[d]	5.212	9.051	7.461	91.83	104.97	89.77
5	Weck et al., 2015[e]	5.177	8.985	7.329	91.95	105.22	89.82
6	Richard and Rendtorff, 2019[f]	5.174	8.985	7.391	91.684	105.128	89.755
7	This Work	5.178	8.991	7.345	91.610	104.786	89.771

[a] Experimental, neutron powder diffraction data.
[b] Experimental, low-temperature (1.5 K) neutron powder diffraction data.
[c] Computational, PBEsol functional.
[d] Computational, PBE-GGA functional.
[e] Computational, DFT corrected for dispersion (DFT-D2) with the PBE-GGA functional.
[f] Computational, Wu-Cohen (WC) modified PBE-GGA functional.

Table 2
Selected bond lengths (Å) from the unit cell of kaolinite.

Bond	Bish, 1993[a]	Richard and Rendtorff, 2019[b]	This Work
OH(1)	0.975(4)	0.976	0.987
OH(2)	0.982(4)	0.973	0.983
OH(3)	0.976(4)	0.975	0.985
OH(4)	0.975(4)	0.974	0.984
Al(1)-O(1)	1.927(6)	1.963	1.965
Al(1)-O(2)	1.930(6)	2.025	2.032
Al(1)-OH(1)	1.913(6)	1.934	1.937
Al(1)-OH(2)	1.890(6)	1.860	1.861
Al(1)-OH(3)	1.865(6)	1.852	1.854
Al(1)-OH(4)	1.915(6)	1.852	1.853
Al(2)-O(1)	1.931(6)	2.015	2.021
Al(2)-O(2)	1.919(6)	1.949	1.952
Al(2)-OH(1)	1.912(6)	1.931	1.933
Al(2)-OH(2)	1.896(6)	1.861	1.862
Al(2)-OH(3)	1.886(6)	1.858	1.859
Al(2)-OH(4)	1.910(6)	1.856	1.858
Si(1)-O(1)	1.618(4)	1.612	1.613
Si(1)-O(3)	1.611(4)	1.636	1.640
Si(1)-O(4)	1.620(4)	1.633	1.645
Si(1)-O(5)	1.619(4)	1.641	1.637
Si(2)-O(2)	1.612(4)	1.609	1.610
Si(2)-O(3)	1.617(4)	1.639	1.643
Si(2)-O(4)	1.616(4)	1.632	1.639
Si(2)-O(5)	1.608(4)	1.635	1.637

[a] Low-temperature (1.5 K) neutron powder diffraction data.
[b] Variable cell-relaxed parameters, WC modified PBE-GGA.

overestimates a, b, and c by between 1.0% and 1.3% compared to the experimental parameters reported in Young and Hewat (1988). The largest deviations for DFT-D2 and DFT performed at the WC modified PBE-GGA level are, on the other hand, 0.77% and 0.62%, respectively. Furthermore, as shown in Table 2, all calculated bond lengths are within 0.05 Å of the experimental values, with the exception of the Al—O subsurface bonds, which are overestimated by up to 0.1 Å. This deviation is again in excellent agreement with the bond lengths previously computed and reported in Richard and Rendtorff (2019).

The electronic band structure and projected density of states (PDOS) for bulk kaolinite provides additional insight into this rigid structure, specifically the orbital compositions of bonding and antibonding interactions. As shown in Fig. 2b, bulk kaolinite has a direct band gap of 4.87 eV that occurs at the Γ point, meaning both the highest occupied and lowest unoccupied molecular orbitals (HOMO and LUMO, respectively) can be found at the Γ point. The occupied states, with a total bandwidth of 8 eV (located from approximately −10 to −2 eV), correspond to molecular orbitals with significant contributions from the O 2p orbitals. The O 2p orbitals align with both the Al and Si 3p states and show the most dominant peaks at −3.5 eV. This peak is composed mostly of O 2p character, indicating charge transfer and a strong bonding network with covalent composition between Al—O, Si—O, and H—O. Contributions from the H 1 s orbital mixing are apparent around −8.5 eV, indicative of O—H bond character. In this region, there is a significant amount of ionic bonding in which the O 2p orbitals mix with the Al and Si 3p orbitals. The LUMO consists primarily of equal contributions from the Al and Si 3p with mixing from the H 1 s and Si 3 s states.

3.2. Kaolinite surface

Using the optimized kaolinite unit cell discussed above, a 2x1x1 periodic surface slab was generated (Fig. 3a) for use in surface-adsorbate interaction calculations. The 2x1x1 surface slab structure was found to have sufficient surface area to accommodate the chosen adsorbates without affecting the calculated adsorption energies (vide infra). The slab height is 5.49 Å along the c-axis, and 20.23 Å of vacuum was added above the alumina (001) surface in order to avoid interactions between slabs within the repeat boundary condition. This resulted in a 10.36 Å × 8.99 Å × 25.72 Å surface structure with 68 atoms total. Table 3 compares selected bond lengths in the bulk kaolinite structure and the 2x1x1 periodic surface slab. As shown, the most significant change is the shortening of the Al—O bonds, specifically Al(1)-O(2) and Al(2)-O(1), in the surface structure, which is consistent with the bulk data presented in Table 2. The Al-O(H) bonds to the exposed hydroxyl groups on the alumina surface – OH(2), OH(3), and OH(4) – are, on the other hand, approximately 0.4 Å longer in the surface structure, although the lengths of the corresponding O—H bonds change only minimally. This is most likely due to the interruption of the hydrogen bonds between the hydroxylated (001) surface and the siloxane (00–1) surface directly above it that occurs when cleaving bulk kaolinite to model the surface. In creating a surface of kaolinite, both the surface states and electronic structure change as a result of being exposed to vacuum, and this is most evident by an increase in total H 1 s contribution to the LUMO as well as the number of distinct H 1 s surface states. In the bulk to surface transformation, two thirds of the surface protons remain vertical (H-up in Fig. 3b) and one third adopt a horizontal orientation (H-dn in Fig. 3b). This rearrangement of surface H is consistent with prior DFT investigations on hydrated surfaces of α-Al_2O_3 (0001) surfaces (Hass, 1998; Hass et al., 2000). Breaking the bonds between kaolinite layers leaves the alumina surface in an undercoordinated arrangement, where one third of the surface H are brought closer to the surface to alleviate undercoordination. This change also creates subtle differences in the electronic band structure of the surface; additional peaks localized in the region of −4 to −8 eV in the valence band (VB) as well as distinct surface H states found in the conduction band (CB) of the PDOS between 3 and 6 eV can be seen in Fig. 3b. The filled states of the surface also appear flatter than in the bulk, further indicative of delocalized electron density across the surface oxygens. Inspection of the empty states shows overlap between the unfilled H 1 s orbitals and the unfilled s and p states of Al and Si. The surface H states found in the CB between 3 and 6 eV are also in agreement with previous studies of the electronic structure of native kaolinite using the WC-GGA (Richard and Rendtorff, 2019) or GGA-PBE (Nisar et al., 2011) exchange-correlation functional.

Table 3
Selected bond lengths (Å).

Bond	Bulk	Surface
OH(1)	0.987	0.982
OH(2)	0.983	0.976
OH(3)	0.985	0.976
OH(4)	0.984	0.988
Al(1)-O(1)	1.965	1.932
Al(1)-O(2)	2.032	1.941
Al(1)-OH(1)	1.937	1.893
Al(1)-OH(2)	1.861	1.910
Al(1)-OH(3)	1.854	1.919
Al(1)-OH(4)	1.853	1.918
Al(2)-O(1)	2.021	1.941
Al(2)-O(2)	1.952	1.932
Al(2)-OH(1)	1.933	1.893
Al(2)-OH(2)	1.862	1.919
Al(2)-OH(3)	1.859	1.910
Al(2)-OH(4)	1.858	1.918
Si(1)-O(1)	1.613	1.642
Si(1)-O(3)	1.640	1.624
Si(1)-O(4)	1.645	1.630
Si(1)-O(5)	1.637	1.626
Si(2)-O(2)	1.610	1.642
Si(2)-O(3)	1.643	1.630
Si(2)-O(4)	1.639	1.624
Si(2)-O(5)	1.637	1.626

3.3. Surface adsorption events on native kaolinite (001) surface

In order to investigate the interactions between a native kaolinite surface and a representative set of adsorbates, we calculated the adsorption energy (E_a in Eq. (1)) as follows:

$$E_a = E_{system} - (E_{adsorbent} + E_{adsorbate}) \quad (1)$$

where E_{system} is the energy of the kaolinite surface with the adsorbate present, $E_{adsorbent}$ is the energy of just the kaolinite surface, and $E_{adsorbate}$ is the energy of the adsorbate in a vacuum. In this work, only the interactions between the alumina (001) surface of kaolinite and the full set of adsorbates are studied, as previous studies have shown that adsorption energies are generally larger on the alumina as compared to the siloxane (00–1) surface (Lee et al., 2013; Han et al., 2016; Li et al., 2018; Chen et al., 2019; Liu et al., 2019). The interactions between the

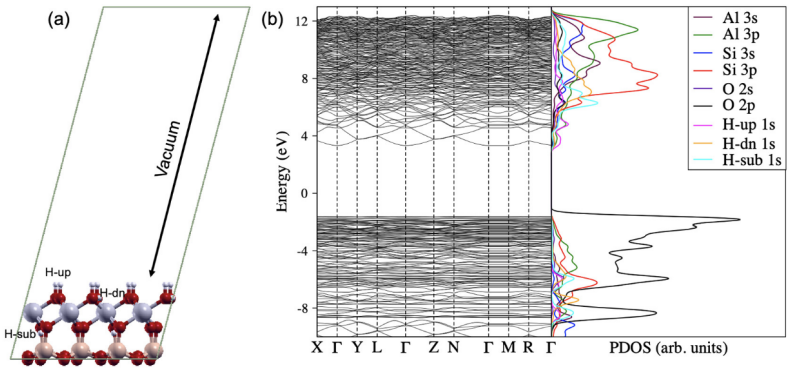

Fig. 3. (a) The 2x1x1 periodic surface slab, as viewed along the b-axis. (b) The electronic band structure (left) and PDOS (right) of the 2x1x1 kaolinite surface slab. An indirect bandgap of 4.59 eV was calculated. The presence of an additional strong peak at −6 eV of the occupied states, as compared to the bulk structure, suggests a change in the O—H bonding in the native surface. The difference in the PDOS between the surface H that are oriented up (H-up) and down (H-dn) is shown here.

siloxane surface of kaolinite and three specific adsorbates (H_2S, SO_2, and SO_3) are analyzed in the Supplemental Materials. The adsorbates are grouped into three categories: (1) protic acids, (2) their corresponding sodium salts, and (3) common small molecule pollutants. Sodium salts were chosen in order to probe the complex bonding effects of common alkali cations on a hydrated clay mineral surface. The constituents of our adsorbate set are different than conventional adsorbates such as metal cations and inner-sphere polyatomic cations (e.g. phosphate), which can easily be placed above the top, hollow, or bridge sites on a surface. Since our adsorbates have significantly different geometries when compared to one another (e.g. planar vs. tetrahedral), they are all initially positioned such that the central atom is directly above one of the top site oxygens on the kaolinite surface and then relaxed. Table 4 lists the adsorbates as well as their calculated adsorption energies on the 2x1x1 kaolinite surface slab, and Fig. 4 shows the interactions observed in Entries 2, 3, and 9. The surface interactions observed in the other fifteen entries – including a comparison of the three H_2SO_3 configurations – are depicted in the Supplemental Materials. For H_2SO_3, we explored (1) a different initial rotation of the adsorbate relative to the surface (Table 4, Entry 6) and (2) the orientation of the proton on the sulfur central atom towards the surface (Table 4, Entry 13) to gauge these effects on surface deprotonation. Each adsorption investigated is an exothermic process, as only negative adsorption energies are observed. All adsorptions also involve multiple hydrogen bonds, ranging from six with $NaHSO_3$ (Table 4, Entry 1) to two with CH_2O, NH_3, O_3, and CO_2 (Table 4, Entries 14–16 and 18). Throughout this series of small molecules, increased numbers of hydrogen bonding events correspond to more negative adsorption energies (i.e. a stronger interaction between the surface and the adsorbate). This indicates that the adsorption energies listed in Table 4 represent the summation of the total interactions present in each scenario. More hydrogen bonds mean more interactions total, which in turn means a more negative adsorption energy.

In addition to hydrogen bonds, the stronger adsorptions have additional bonding events such as proton abstraction or Na—O interactions. In the case of proton abstractions (H_2SO_3 and HNO_3; Table 4, Entries 5–6 and 10), the surface functional groups change from Al-OH to Al-OH_2, indicating that oxyanions with a positively charged main group center will aid in the formation of surface waters via acid-base chemistry. Notably, in each protic acid/sodium salt pairing, the sodium salt variant has more negative adsorption energy than the corresponding protic acid. For example, there is an approximately 20 kcal mol^{-1} difference between the adsorption of formic acid (HCOOH; Table 4, Entry 9; Fig. 4a) and sodium formate (HCOONa; Table 4, Entry 2; Fig. 4b). Table 4 also highlights that sulfur-containing adsorbates – specifically adsorbates in which the sulfur atom has a positive oxidation state – impact the kaolinite surface more than the other adsorbates in each category. Sodium bisulfite ($NaHSO_3$; Table 4, Entry 1) has the most negative adsorption energy of all the adsorbates probed in this study, by about 45 kcal mol^{-1}. We hypothesize that this is due to the presence of both Na—O interactions and six hydrogen bonds between the kaolinite surface and the bisulfite anion. Likewise, sulfonic acid in two of the three configurations sampled (H_2SO_3; Table 4, Entries 5 and 6) is the protic acid with the most negative adsorption energy, again due to the presence of both multiple hydrogen bonds and proton abstraction. As a final example, sulfur trioxide (SO_3; Table 4, Entry 3; Fig. 4c) is the small molecule pollutant that most strongly interacts with the kaolinite surface. In fact, it significantly changes the surface. The SO_3 molecule abstracts a hydroxyl group from the surface to generate an HSO_4^- anion, a transformation that parallels the hydration of SO_3 to generate sulfuric acid in the formation of acid rain. The adverse effects observed here support previously reported results that sulfur compounds are a concern within cultural heritage, as they can promote degradation pathways and cause the deterioration of pigments (Coccato et al., 2017), stone monuments and buildings (Diana et al., 2007; Belfiore et al., 2013), and paper (Williams and Grosjean, 1992). Interestingly, hydrogen sulfide – which also has a central sulfur atom, but with a negative oxidation state – only weakly interacts with the surface via hydrogen bonding. No extra events or significant surface perturbations are observed.

Table 4
Adsorption energies on the native kaolinite (001) surface, ranked by magnitude.

Entry	Adsorbate	Configuration	E_a (eV)	E_a (kcal mol^{-1})	Interactions Between Adsorbate and Surface
1	$NaHSO_3$	–	−3.72	−85.68	H-bonding (6); Na—O interactions
2	HCOONa	–	−1.73	−39.81	H-bonding (3); Na—O interactions
3	SO_3	–	−1.71	−39.49	H-bonding; SO_3 abstracting OH^- to form HSO_4^- anion
4	$NaNO_3$	–	−1.57	−36.23	H-bonding (3); Na—O interactions
5	H_2SO_3	1	−1.46	−33.74	H-bonding; H^+ abstracted from acid to form H_2O on surface
6	H_2SO_3	2	−1.28	−29.41	H-bonding; H^+ abstracted from acid to form H_2O on surface
7	$NaHCO_3$	–	−1.17	−26.87	H-bonding (4); Na—O interactions
8	H_2CO_3	–	−0.98	−22.55	H-bonding (4)
9	HCOOH	–	−0.94	−21.79	H-bonding (4)
10	HNO_3	–	−0.80	−18.47	H-bonding; H^+ abstracted from acid
11	SO_2	–	−0.74	−17.05	H-bonding (3)
12	H_2O	–	−0.65	−14.96	H-bonding (3)
13	H_2SO_3	3	−0.61	−13.98	H-bonding (3)
14	CH_2O	–	−0.48	−10.98	H-bonding (2)
15	NH_3	–	−0.43	−9.96	H-bonding (2)
16	O_3	–	−0.32	−7.37	H-bonding (2)
17	H_2S	–	−0.30	−6.97	H-bonding (3)
18	CO_2	–	−0.25	−5.69	H-bonding (2)

In order to further understand the molecular interactions between the native hydrated kaolinite surface and this series of adsorbates, we also analyzed the band structure, PDOS, and charge density of one adsorption in each category: (1) formic acid, (2) sodium formate, and (3) sulfur trioxide. For ease of comparison, the electronic band structures of the three selected adsorptions are in the Supplemental Materials (Figs. S1, S2, and S3), next to their corresponding PDOS. The interactions between the kaolinite surface and HCOOH (Figs. 4a) do not drastically change the nature or size of the band gap, as there is still a direct band gap at the Γ point that has only changed by 0.05 eV with the adsorption of HCOOH. The formic acid adsorbate has O 2 s and 2p character that overlaps with the O 2 s and O 2p character of the kaolinite surface, and the same is true of the H 1 s interaction present in both the occupied and unoccupied states (Fig. 4d). The native surface and the surface + HCOOH differ, however, by the addition of C 2p bonding and antibonding character. The bonding interactions between C and O 2p are present in the PDOS within the same energy range of the O 2p bonding interactions with the Al and Si 3p. The most prominent new peak for C (cyan line in Fig. 4d) is found in the LUMO for the kaolinite surface + HCOOH interaction and is the antibonding C and O 2p molecular orbitals at approximately 2 eV.

Interactions between sodium formate (HCOONa) and the kaolinite surface follow similar trends to those observed in the kaolinite surface + HCOOH structure. The electronic band structure of the surface + HCOONa retains a direct bandgap at the Γ point with a shift of 0.15 eV compared to the native surface in Fig. 3b. Mixing between the native surface and the Na 3 s is mostly absent in the occupied states displayed here, as the Na—O bonds are found below −10 eV. We find most of the Na states in the LUMO, shown as the magenta Na 3 s line in Fig. 4e.

The most substantial changes in the electronic band structure of native kaolinite follow its interaction with SO_3. In the kaolinite surface

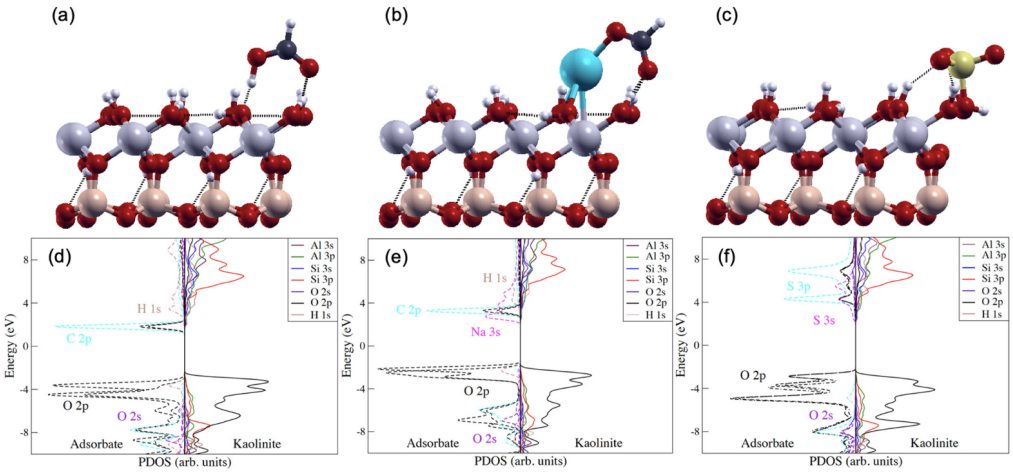

Fig. 4. Kaolinite surface + (a) HCOOH, (b) HCOONa, or (c) SO_3, as viewed along the b-axis. Carbon, sodium, and sulfur are shown in dark gray, teal, and yellow, respectively, and hydrogen bonding is shown in black. (b) PDOS of the kaolinite surface + (d) HCOOH, (e) HCOONa, or (f) SO_3.

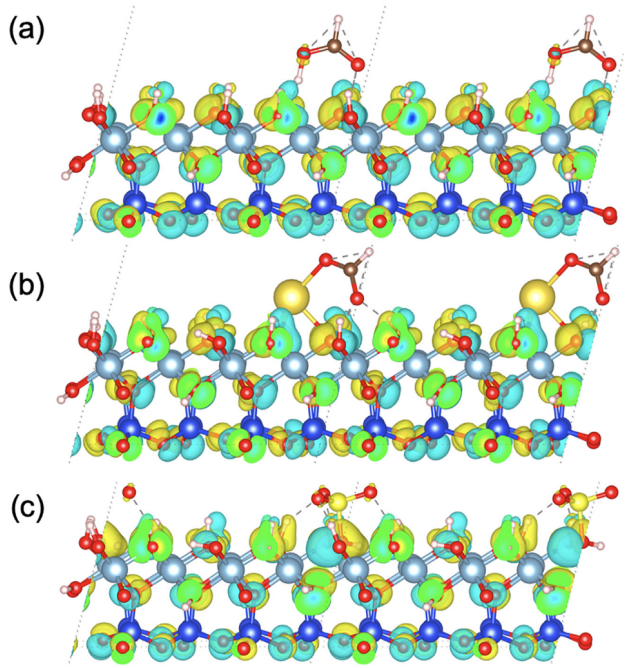

Fig. 5. Charge density difference plots for (a) HCOOH, (b) HCOONa, and (c) SO_3 adsorptions. The yellow color represents positive charge density (i.e. more charge density when the adsorbate is present), and the aqua blue color represents negative charge density (i.e. more charge density when the adsorbate is not present). For clarity, the charge density on the adsorbate has been subtracted out of the figure.

+ SO_3 structure, we see a direct band gap at the Γ point that has undergone a considerable shift of 0.70 eV relative to Fig. 3b. In the occupied states, the overlap of the S 3p with the O 2p and Si 3p of the native surface suggests ionic S—O bonding interaction between the S 3p, O 2p, and O 2 s states of SO_3 and the O 2p and Si 3p of the surface (Fig. 4f). Significant orbital mixing between the S 3p and Si 3p is present in the unoccupied states with S 3 s and O 2p character, further substantiating the presence of S—O bonds that differ from previously discussed surface interactions. The strength and scope of the S—O bonding interactions occurring between SO_3 and the kaolinite surface are likely responsible for the considerable shift in total band gap, as compared to kaolinite + HCOOH or HCOONa.

Fig. 5 compares the charge density difference plots for the three selected adsorptions shown in Fig. 4: the kaolinite surface interacting with (a) HCOOH, (b) HCOONa, and (c) SO_3. As illustrated, the charge density resides on the oxygen atoms (red spheres) along the surface, not on the cationic aluminum (light blue spheres) and silicon (dark blue spheres) atoms. This is true for all three examples. Formic acid (Fig. 5a) only interacts with the surface via weak hydrogen bonds. The adsorption is not strong enough to perturb the atoms on the kaolinite surface, which is common with hydrated edge-sharing octahedra and a weak outer sphere adsorption. More significant changes in the charge density are seen in the HCOONa adsorption (Fig. 5b), where the more drastic shifts are localized around the sodium cation, as evidenced by an increase in the size of the aqua blue charge densities. This is a localized effect in which the sodium cation-surface bond perturbations do not cascade across the surface. Fig. 5b also demonstrates that the cation can anchor the anion to the kaolinite surface, an effect that may have additional consequences such as salt nucleation or saponification on clay mineral surfaces. Lastly, the SO_3 adsorption is shown in Fig. 5c. As mentioned above, SO_3 abstracts a hydroxyl group from the kaolinite surface to form a HSO_4^- anion. Consequently, there are significant surface perturbations all along the alumina surface, as the loss of a surface hydroxyl group causes a complete restructuring of the charge density of both the surface and subsurface oxygen atoms. Here, the SO_3-kaolinite surface interaction is delocalized in nature and manifests as a collective effect, which is significantly different than either the HCOOH or HCOONa example.

3.4. Surface adsorption events on native kaolinite (001) surface in the presence of explicit water molecules

In order to explore the effect of explicit hydration on the kaolinite surface structure and adsorbate bonding interactions, we calculated the adsorption energies for the same set of adsorbates in the presence of six water molecules. Table 5 lists the obtained values for the small molecules and pollutants, and Fig. 6 shows the interactions observed in Entries 1 and 8. The surface interactions observed in the other seven entries – including comparisons of the two $SO_2{\cdot}6H_2O$ (Entries 2 and 6) and two $CH_2O{\cdot}6H_2O$ (Entries 5 and 7) configurations – are depicted in the Supplemental Materials. For $SO_2{\cdot}6H_2O$ and $CH_2O{\cdot}6H_2O$, we investigated the effect of interrupting the hydrogen bonding network of the water molecules with the kaolinite surface and inserting the adsorbate directly into that network (Table 5, Entries 6 and 7). In both cases, this resulted in a weaker adsorption energy. As a hydrated form of alumina resembling gibbsite, the kaolinite surface responds strongly to the addition of water; significant hydrogen bonding with these additional molecules occurs in all calculations. We find that for some configurations, the water molecules actually push nonpolar, gaseous molecules such as CO_2 away from the surface (Fig. 6a; Table 5, Entry 1), as the hydroxyl groups on kaolinite prefer to interact with the polar water molecules. More polar small molecules such as H_2S are, on the other, integrated into the hydrogen bonding network that the six water molecules form on the kaolinite surface (Fig. 6b; Table 5, Entry 8). For all adsorbates listed in Table 5 (except SO_3), the adsorption energy is significantly more negative in the presence of six explicit water molecules, often by 30 to 40 kcal mol^{-1}, when compared to the values presented in Table 4.

Table 5
Adsorption energies on the native kaolinite surface in the presence of 6 H_2O molecules.

Entry	Adsorbate	Configuration	E_a (eV)	E_a (kcal mol^{-1})
1	$CO_2{\cdot}6H_2O$	–	−2.30	−52.95
2	$SO_2{\cdot}6H_2O$	1	−2.28	−52.66
3	$NH_3{\cdot}6H_2O$	–	−2.27	−52.36
4	$O_3{\cdot}6H_2O$	–	−2.07	−47.71
5	$CH_2O{\cdot}6H_2O$	1	−1.86	−42.89
6	$SO_2{\cdot}6H_2O$	2	−1.75	−40.40
7	$CH_2O{\cdot}6H_2O$	2	−1.63	−37.70
8	$H_2S{\cdot}6H_2O$	–	−1.59	−36.69
9	$SO_3{\cdot}6H_2O$	–	−1.25	−28.76

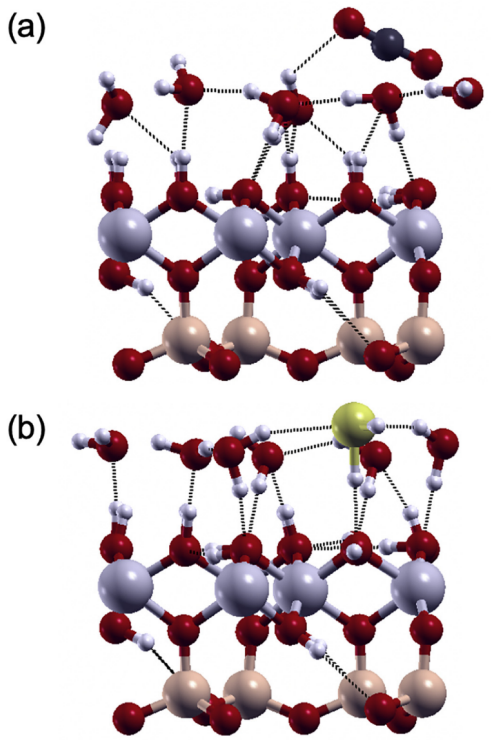

Fig. 6. The 2x1x1 kaolinite slab +6 H_2O + (a) CO_2 or (b) H_2S, as viewed along the a-axis. Hydrogen bonding is shown in black.

Fig. 7 illustrates the effect of explicit hydration on the adsorption of protic acids and sodium salts. Sideview images of the configurations for these adsorption events are provided in the Supplemental Materials. As discussed above for the small molecule adsorptions in vacuum, the sodium salt generally has a more negative adsorption energy than the corresponding protic acid. The only exception is $H_2CO_3{\cdot}6H_2O$ and $NaHCO_3{\cdot}6H_2O$, which differ by approximately 1 kcal mol^{-1}. Additionally, in most cases, the hydrated adsorbate has a more negative adsorption energy than the non-hydrated variant. This parallels the trend observed in the small molecule series. The only exception to the trend here is $NaHSO_4$, which, as noted earlier, is hypothesized to have

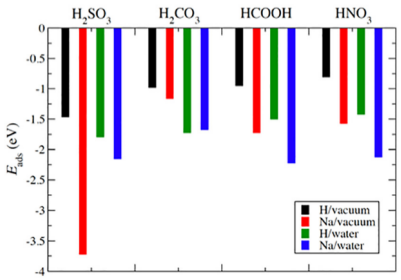

Fig. 7. Comparison of the adsorption energies for the protic acid and sodium salt series, both in vacuum and with explicit hydration.

such a large (negative) adsorption energy due to the presence of both strong Na—O interactions and six hydrogen bonds between the surface and the bisulfite anion in its adsorption conformation. In the hydrated scenarios, almost all of the adsorbates once again have increased hydrogen bonding with the kaolinite surface. Additional adsorption events such as Na—O interactions and proton abstractions are also observed in the presence of explicit hydration, but due to the increased hydrogen bonding with the six additional water molecules, these events appear to be less important in predicting the strength of the surface interaction.

3.5. Adsorption events on partially dehydrated kaolinite (001) surface

The native (fully hydrated) kaolinite surface modeled above represents a completely unfired porcelain object, a type of artifact that may not be frequently encountered in cultural heritage. Rather, porcelain is generally fired in a kiln at temperatures between 1200 and 1400 °C to undergo a series of chemical and structural transformations and form a hard, vitrified object containing acicular mullite, an aluminosilicate mineral with its own unique properties (Carty and Senapati, 1998; Hsiung et al., 2013; Andrini et al., 2016). In order to probe how the removal of water from the kaolinite surface (in, for example, the first steps of the firing process) impacts the adsorption of small molecules or acids, we also modeled a partially dehydrated kaolinite surface in which one water molecule has been removed (Fig. 8). The kaolinite surface undergoes a significant restructuring to compensate for the loss of the water molecule. Specifically, the remaining hydroxyl groups bend closer towards the surface to weakly interact with the now deprotonated oxygen, which creates a flatter surface. Similarly, the aluminum atom from which the hydroxyl group is removed also shifts in an attempt to regain octahedral coordination.

Now using the partially dehydrated kaolinite surface, we again calculated the adsorption energies of HCOOH, HCOONa, and SO_3. In each case, the adsorption energy became more negative, indicating stronger interactions with the partially dehydrated surface. The following E_a values were obtained for HCOOH, HCOONa, and SO_3, respectively: −39.02 kcal mol^{-1} (−1.69 eV), −38.71 kcal mol^{-1} (−1.68 eV), and −70.32 kcal mol^{-1} (−3.05 eV). Being more basic than the native structure, the partially dehydrated surface deprotonates formic acid (Fig. 9a), an event that does not occur with the hydrated surface (Fig. 4a). In the case of HCOONa, the salt retains the same configuration as in Fig. 4b, but relocates on the surface slab (Fig. 9b). The loss of the surface hydroxyl group causes the sodium cation to move away from the vacancy in order to interact with multiple oxygen atoms. As the anion is anchored to the cation, this too shifts. Lastly, SO_3 undergoes a similar transformation to that observed on the native surface. However, instead of abstracting the hydroxyl group, a proton transfer from the hydroxyl group below the SO_3 sulfur atom to an adjacent (deprotonated) oxygen atom occurs, followed by the direct interaction of the sulfur atom with the now deprotonated oxygen below it on the surface (Fig. 9c). Thus, we do not see the formation of a bisulfate anion (Fig. 4c) here, but rather the binding of the SO_3 to the surface.

4. Conclusions

In conclusion, this work demonstrates how DFT methods can be used to computationally explore the interactions between a representative set of adsorbates and a mineral surface relevant to art conservation. It is intended to complement ongoing studies within the field of cultural heritage devoted to the understanding the complex interactions of clay minerals within, as one example, a natural or artificial patina on an architectural artifact (Calia et al., 2011). The trends delineated here suggest how a kaolinite surface will respond to a range of different environmental conditions and, thus, allow us to create a set of guidelines for the care of unfired porcelain objects. For example, our results provide atomistic information on why relative humidity is important to control when storing or treating objects. Significantly stronger

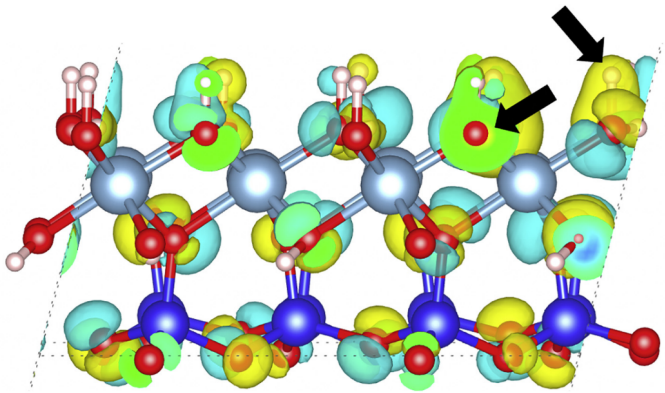

Fig. 8. The charge density difference plot for the partially dehydrated kaolinite surface. The yellow color represents positive charge density (i.e. more charge density on the native hydrated surface), and the aqua blue color represents negative charge density (i.e. more charge density on the partially dehydrated surface). The black arrows identify the —OH and —H that were removed.

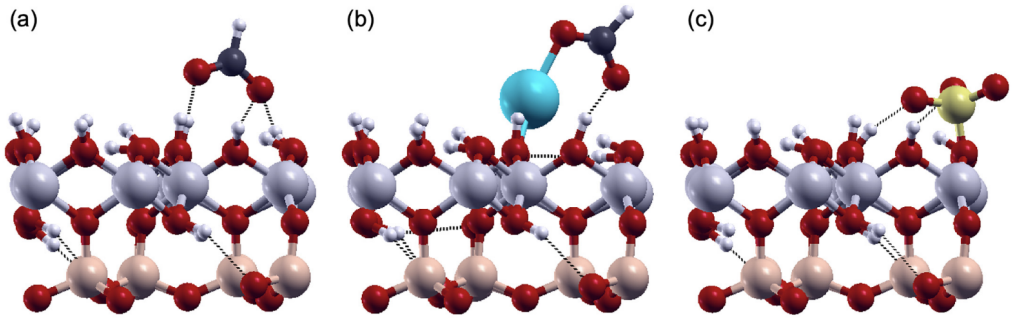

Fig. 9. Adsorption of (a) HCOOH, (b) HCOONa, and (c) SO_3 on the partially dehydrated kaolinite surface, as viewed along the a-axis. Hydrogen bonding is shown in black.

adsorptions are observed in the presence of explicit hydration. Additionally, the two strongest acids studied – sulfonic and nitric acid – are deprotonated by the basic alumina face of kaolinite, leading to the generation of an Al-OH_2 functional group on the surface. The sodium salt adsorptions exhibit both strong Na—O interactions and, in some cases, an anchoring effect in which the sodium cation anchors the anion to the surface, which may have unexplored consequences such as salt nucleation or saponification. Lastly and perhaps most importantly, we identified a class of molecules – those containing a central sulfur atom with a positive oxidation state – as particularly dangerous for kaolinite surfaces, as these molecules strongly adsorb and cause significant surface perturbations. This finding suggests that, if possible, sulfur-containing acids and sulfur-based pollutants such as SO_3 should be avoided or protected against for unfired kaolinite, any exposed surface that contains minerals resembling gibbsite, or other partially hydrated surface terminations.

Furthermore, by removing one water molecule from the kaolinite surface, we begin to understand how dehydration affects how this common material interacts with relevant chemicals. In this work, we observe stronger adsorptions of HCOOH, HCOONa, and SO_3 on the partially dehydrated surface, which may suggest that a more basic surface corresponds to stronger adsorptions. More work, however, is needed to confirm this. Future research will not only further explore the impact of dehydrating and transforming the surface to metakaolin and ultimately mullite to better model the surface interactions between a fired or partially fired porcelain object and common pollutants, but it will also probe the atomistic effects of introducing a glaze on the kaolinite surface.

Data availability

(1) A comparison of the lattice parameters for different open-source software suites and exchange-correlation functionals, (2) the electronic band structures of three selected adsorptions (HCOOH, HCOONa, and SO_3), (3) selected adsorptions (H_2S, SO_2, and SO_3) on the siloxane (00-1) surface of kaolinite, and (4) visualization of each adsorption configuration are provided in the Supplementary Materials.

CRediT authorship contribution statement

Jessica E. Heimann: Visualization, Investigation, Conceptualization, Writing - original draft, Writing - review & editing. **Ryan T. Grimes**: Visualization, Writing - original draft, Writing - review & editing. **Zeev Rosenzweig**: Supervision, Project administration. **Joseph W. Bennett**: Supervision, Project administration, Conceptualization, Writing - original draft, Writing - review & editing

Declaration of Competing Interest

The authors declare that they have no known competing financial interests or personal relationships that could have appeared to influence the work reported in this paper.

Acknowledgements

This research was supported by the Andrew W. Mellon Foundation under Award 41500634 and the Extreme Science and Engineering Discovery Environment (XSEDE) (Towns et al., 2014) grant TG-CHE190075, which is supported by National Science Foundation grant number ACI-1548562. All calculations were performed using the University of Maryland Baltimore County (UMBC) High Performance Computing Facility (HPCF). The acquisition of equipment for the UMBC HPCF is partially supported by the National Science Foundation, whose support we gratefully acknowledge and which requires the following notice: This material is based upon work supported by the National Science Foundation3 under the MRI grants CNS-0821258, CNS-1228778, and OAC-1726023, and the SCREMS grant DMS-0821311. The atomistic pictures and charge density images in this work were generated with XCrySDen (Kokalj, 2003) and VESTA (Momma and Izumi, 2011), respectively.

Appendix A. Supplementary data

Supplementary data to this article can be found online at https://doi.org/10.1016/j.clay.2021.106075.

References

Alshameri, A., He, H., Zhu, J., Xi, Y., Zhu, R., Ma, L., Tao, Q., 2018. Adsorption of ammonium by different natural clay minerals: characterization, kinetics and adsorption isotherms. Appl. Clay Sci. 159, 83–93. https://doi.org/10.1016/j.clay.2017.11.007.

Alstadt, V.J., Kubicki, J.D., Freedman, M.A., 2016. Competitive adsorption of acetic acid and water on kaolinite. J. Phys. Chem. A 120 (42), 8339–8346. https://doi.org/10.1021/acs.jpca.6b06968.

Andrini, L., Gauna, M.R., Conconi, M.S., Suarez, G., Requejo, F.G., Aglietti, E.F., Rendtorff, N.M., 2016. Extended and local structural description of a kaolinitic clay, its fired ceramics and intermediates: an XRD and XANES analysis. Appl. Clay Sci. 124-125, 39–45. https://doi.org/10.1016/j.clay.2016.01.049.

Angelini, M.M., Garrard, R.J., Rosen, S.J., Hinrichs, R.Z., 2007. Heterogeneous reactions of gaseous HNO_3 and NO_2 on the clay minerals kaolinite and pyrophyllite. J. Phys. Chem. A 111 (17), 3326–3335. https://doi.org/10.1021/jp0672656.

Belfiore, C.M., Barca, D., Bonazza, A., Comite, V., La Russa, M.F., Pezzino, A., Ruffolo, S. A., Sabbioni, C., 2013. Application of spectrometic analysis to the identification of pollution sources causing cultural heritage damage. Environ. Sci. Pollut. R. 20, 8848–8859. https://doi.org/10.1007/s11356-013-1810-y.

Bennett, J.W., Bjorklund, J.L., Forbes, T.Z., Mason, S.E., 2017. Systematic study of aluminum nanoclusters and anion adsorbates. Inorg. Chem. 56 (21), 13014–13028. https://doi.org/10.1021/acs.inorgchem.7b01803.

Bennett, J.W., Jones, D.T., Hamers, R.J., Mason, S.E., 2018a. First-principles and thermodynamics study of compositionally tuned complex metal oxides: cation release from the (001) surface of Mn-rich lithium nickel manganese cobalt cxide. Inorg. Chem. 57 (21), 13300–13311. https://doi.org/10.1021/acs.inorgchem.8b01855.

Bennett, J.W., Jones, D., Huang, X., Hamers, R.J., Mason, S.E., 2018b. Dissolution of complex metal oxides from first-principles and thermodynamics: cation removal from the (001) Surface of $Li(Ni_{1/3}Mn_{1/3}Co_{1/3})O_2$. Environ. Sci. Technol. 52 (10), 5792–5802. https://doi.org/10.1021/acs.est.8b00054.

Bennett, J.W., Huang, X., Fang, Y., Cwiertny, D.M., Grassian, V.H., Mason, S.E., 2019. Methane dissociation on α-Fe_2O_3(0001) and Fe_3O_4(111) surfaces: first-principles insights into chemical looping combustion. J. Phys. Chem. C 123 (11), 6450–6463. https://doi.org/10.1021/acs.jpcc.8b08675.

Bennett, J.W., Jones, D.T., Hudson, B.G., Melendez-Rivera, J., Hamers, R.J., Mason, S.E., 2020. Emerging investigator series: first-principles and thermodynamics comparison of compositionally-tuned delafossites: cation release from the (001) surface of complex metal oxides. Environ. Sci. 7 (6), 1642–1651. https://doi.org/10.1039/C9EN01304K.

Bhattacharyya, K.G., Gupta, S.S., 2008. Adsorption of a few heavy metals on natural and modified kaolinite and montmorillonite: a review. Adv. Colloid Interfac. 140 (2), 114–131. https://doi.org/10.1016/j.cis.2007.12.008.

Bish, D.L., 1993. Rietveld refinement of the kaolinite structure at 1.5 K. Clay Clay Miner. 41 (6), 738–744. https://doi.org/10.1346/CCMN.1993.0410613.

Bjorklund, J.L., Bennett, J.W., Forbes, T.Z., Mason, S.E., 2019. Modeling of MAl_{12} keggin heteroatom reactivity by anion adsorption. Cryst. Growth Des. 19 (5), 2820–2829. https://doi.org/10.1021/acs.cgd.9b00044.

Brigatti, M.F., Malferrari, D., Laurora, A., Elmi, C., 2011. Structure and mineralogy of layer silicates: recent perspectives and new trends. In: Layered Mineral Structures and their Application in Advanced Technologies, 11, pp. 1–71. https://doi.org/10.1180/EMU-notes.11.1.

Calia, A., Lettieri, M., Quarta, G., 2011. Cultural heritage study: microdestructive techniques for detection of clay minerals on the surface of historic buildings. Appl. Clay Sci. 53, 525–531. https://doi.org/10.1016/j.clay.2010.10.021.

Carty, W.M., Senapati, U., 1998. Porcelain—raw materials, processing, phase evolution, and mechanical behavior. J. Am. Ceram. Soc. 81 (1), 3–20. https://doi.org/10.1111/j.1151-2916.1998.tb02290.x.

Chen, Y.-H., Lu, D.-L., 2015. CO_2 capture by kaolinite and its adsorption mechanism. Appl. Clay Sci. 104, 221–228. https://doi.org/10.1016/j.clay.2014.11.036.

Chen, J., Min, F.-F., Liu, L., Liu, C., Lu, F., 2017. Experimental investigation and DFT calculation of different amine/ammonium salts adsorption on kaolinite. Appl. Surf. Sci. 419, 241–251. https://doi.org/10.1016/j.apsusc.2017.04.213.

Chen, G., Li, X., Zhou, L., Xia, S., Yu, L., 2019. Mechanism insights into Hg(II) adsorption on kaolinite(001) surface: a density functional study. Appl. Surf. Sci. 488, 494–502. https://doi.org/10.1016/j.apsusc.2019.05.227.

Coccato, A., Moens, L., Vandenabeele, P., 2017. On the stability of mediaeval inorganic pigments: a literature review of the effect of climate, material selection, biological activity, analysis and conservation treatments. Herit. Sci. 5 (12) https://doi.org/10.1186/s40494-017-0125-6.

Corum, K.W., Huang, X., Bennett, J.W., Mason, S.E., 2017. Systematic density functional theory study of the structural and electronic properties of constrained and fully relaxed (001) surfaces of alumina and hematite. Mol. Simul. 43 (5–6), 406–419. https://doi.org/10.1080/08927022.2017.1285402.

Corum, K.W., Abbaspour Tamijani, A., Mason, S.E., 2018. Density functional theory study of arsenate adsorption onto alumina surfaces. Minerals 8 (3). https://doi.org/10.3390/min8030091.

Cygan, R.T., Greathouse, J.A., Heinz, H., Kalinichev, A.G., 2009. Molecular models and simulations of layered materials. J. Mater. Chem. 19, 2470–2481. https://doi.org/10.1039/B819076C.

Diana, M., Gabrielli, N., Ridolfi, S., 2007. Sulfur determination on stone monuments with a transportable EDXRF system. X-Ray Spectrom. 36 (6), 424–428. https://doi.org/10.1002/xrs.1005.

Garrity, K.F., Bennett, J.W., Rabe, K.M., Vanderbilt, D., 2014. Pseudopotentials for high-throughput DFT calculations. Comput. Mater. Sci. 81, 446–452. https://doi.org/10.1016/j.commatsci.2013.08.053.

Giannozzi, P., Baroni, S., Bonini, N., Calandra, M., Car, R., Cavazzoni, C., Ceresoli, D., Chiarotti, G.L., Cococcioni, M., Dabo, I., Dal Corso, A., de Gironcoli, S., Fabris, S., Fratesi, G., Gebauer, R., Gerstmann, U., Gougoussis, C., Kokalj, A., Lazzeri, M., Martin-Samos, L., Marzari, N., Mauri, F., Mazzarello, R., Paolini, S., Pasquarello, A., Paulatto, L., Sbraccia, C., Scandolo, S., Sclauzero, G., Seitsonen, A.P., Smogunov, A., Umari, P., Wentzcovitch, R.M., 2009. QUANTUM ESPRESSO: a modular and open-source software project for quantum simulations of materials. J. Phys.-Condens. Mat. 21 (39), 395502. https://doi.org/10.1088/0953-8984/21/39/395502.

Giannozzi, P., Andreussi, O., Brumme, T., Bunau, O., Buongiorno Nardelli, M., Calandra, M., Car, R., Cavazzoni, C., Ceresoli, D., Cococcioni, M., Colonna, N., Carnimeo, I., Dal Corso, A., de Gironcoli, S., Delugas, P., DiStasio, R.A., Ferretti, A., Floris, A., Fratesi, G., Fugallo, G., Gebauer, R., Gerstmann, U., Giustino, F., Gorni, T., Jia, J., Kawamura, M., Ko, H.Y., Kokalj, A., Küçükbenli, E., Lazzeri, M., Marsili, M., Marzari, N., Mauri, F., Nguyen, N.L., Nguyen, H.V., Otero-de-la-Roza, A., Paulatto, L., Poncé, S., Rocca, D., Sabatini, R., Santra, B., Schlipf, M., Seitsonen, A.P., Smogunov, A., Timrov, I., Thonhauser, T., Umari, P., Vast, N., Wu, X., Baroni, S., 2017. Advanced capabilities for materials modelling with Quantum ESPRESSO. J. Phys.-Condens. Mat. 29 (46), 465901. https://doi.org/10.1088/1361-648x/aa8f79.

Goffinet, C.J., Mason, S.E., 2012. Comparative DFT study of inner-sphere As(III) complexes on hydrated α-Fe_2O_3(0001) surface models. J. Environ. Monit. 14 (7), 1860–1871. https://doi.org/10.1039/C2EM30355H.

Han, Y., Liu, W., Chen, J., 2016. DFT simulation of the adsorption of sodium silicate species on kaolinite surfaces. Appl. Surf. Sci. 370, 403–409. https://doi.org/10.1016/j.apsusc.2016.02.179.

Hass, K.C., 1998. The chemistry of water on alumina surfaces: reaction dynamics from first principles. Science 282 (5387), 265–268. https://doi.org/10.1126/science.282.5387.265.

Hass, K.C., Schneider, W.F., Curioni, A., Andreoni, W., 2000. First-principles molecular dynamics simulations of H2O on α-Al2O3(0001). J. Phys. Chem. B 104 (23), 5527–5540. https://doi.org/10.1021/jp000040p.

He, M.-C., Zhao, J., Wang, S.-X., 2013. Adsorption and diffusion of Pb(II) on the kaolinite (001) surface: a density-functional theory study. Appl. Clay Sci. 85, 74–79. https://doi.org/10.1016/j.clay.2013.08.045.

Heinz, H., 2006. Interaction energy and surface reconstruction between sheets of layered silicates. J. Chem. Phys. 124, 224713. https://doi.org/10.1063/1.2202330.

Heinz, H., Suter, U.W., 2004. Surface structure of organoclays. Angew. Chem. Int. Ed. 43 (17), 2239–2243. https://doi.org/10.1002/anie.200352747.

Hohenberg, P., Kohn, W., 1964. Inhomogeneous electron gas. Phys. Rev. 136 (3B), B864–B871. https://doi.org/10.1103/PhysRev.136.B864.

Hsiung, C.-H.H., Pyzik, A.J., De Carlo, F., Xiao, X., Stock, S.R., Faber, K.T., 2013. Microstructure and mechanical properties of acicular mullite. J. Eur. Ceram. Soc. 33 (3), 503–513. https://doi.org/10.1016/j.jeurceramsoc.2012.09.017.

Hu, X.L., Michaelides, A., 2008. Water on the hydroxylated (001) surface of kaolinite: from monomer adsorption to a flat 2D wetting layer. Surf. Sci. 602 (4), 960–974. https://doi.org/10.1016/j.susc.2007.12.032.

Hu, X.L., Michaelides, A., 2010. The kaolinite (001) polar basal plane. Surf. Sci. 604 (2), 111–117. https://doi.org/10.1016/j.susc.2009.10.026.

Huang, X., Bennett, J.W., Hang, M.N., Laudadio, E.D., Hamers, R.J., Mason, S.E., 2017. Ab initio atomistic thermodynamics study of the (001) surface of $LiCoO_2$ in a water environment and implications for reactivity under ambient conditions. J. Phys. Chem. C 121 (9), 5069–5080. https://doi.org/10.1021/acs.jpcc.6b12163.

Jain, A., Shin, Y., Persson, K.A., 2016. Computational predictions of energy materials using density functional theory. Nat. Rev. Mater. 1 (1), 15004. https://doi.org/10.1038/natrevmats.2015.4.

Jones, R.O., 2015. Density functional theory: its origins, rise to prominence, and future. Rev. Mod. Phys. 87 (3), 897–923. https://doi.org/10.1103/RevModPhys.87.897.

Kohn, W., Sham, L.J., 1965. Self-consistent equations including exchange and correlation effects. Phys. Rev. 140 (4A), A1133–A1138. https://doi.org/10.1103/PhysRev.140.A1133.

Kokalj, A., 2003. Computer graphics and graphical user interfaces as tools in simulations of matter at the atomic scale. Comput. Mater. Sci. 28 (2), 155–168. https://doi.org/10.1016/S0927-0256(03)00104-6.

Kremleva, A., Krüger, S., Rösch, N., 2008. Density functional model studies of uranyl adsorption on (001) surfaces of kaolinite. Langmuir 24 (17), 9515–9524. https://doi.org/10.1021/la801278j.

Kubicki, J.D., Kwon, K.D., Paul, K.W., Sparks, D.L., 2007. Surface complex structures modelled with quantum chemical calculations: carbonate, phosphate, sulphate, arsenate and arsenite. Eur. J. Soil Sci. 58 (4), 932–944. https://doi.org/10.1111/j.1365-2389.2007.00931.x.

Kubicki, J.D., Halada, G.P., Jha, P., Phillips, B.L., 2009. Quantum mechanical calculation of aqueuous uranium complexes: carbonate, phosphate, organic and biomolecular species. Chem. Cent. J. 3 (1), 10. https://doi.org/10.1186/1752-153X-3-10.

Lee, S.G., Choi, J.I., Koh, W., Jang, S.S., 2013. Adsorption of β-D-glucose and cellobiose on kaolinite surfaces: density functional theory (DFT) approach. Appl. Clay Sci. 71, 73–81. https://doi.org/10.1016/j.clay.2012.11.002.

Li, Z., Gallus, L., 2007. Adsorption of dodecyl trimethylammonium and hexadecyl trimethylammonium onto kaolinite — competitive adsorption and chain length effect. Appl. Clay Sci. 35 (3), 250–257. https://doi.org/10.1016/j.clay.2006.09.004.

Li, Z., Schulz, L., Ackley, C., Fenske, N., 2010. Adsorption of tetracycline on kaolinite with pH-dependent surface charges. J. Colloid Interface Sci. 351 (1), 254–260. https://doi.org/10.1016/j.jcis.2010.07.034.

Li, B., Liu, S., Zhang, L., 2018. Interaction between low rank coal and kaolinite particles: a DFT simulation. Appl. Surf. Sci. 456, 215–220. https://doi.org/10.1016/j.apsusc.2018.06.121.

Liu, L., Min, F., Chen, J., Lu, F., Shen, L., 2019. The adsorption of dodecylamine and oleic acid on kaolinite surfaces: insights from DFT calculation and experimental investigation. Appl. Surf. Sci. 470, 27–35. https://doi.org/10.1016/j.apsusc.2018.11.104.

Martorell, B., Kremleva, A., Krüger, S., Rösch, N., 2010. Density functional model study of uranyl adsorption on the solvated (001) surface of kaolinite. J. Phys. Chem. C 114 (31), 13287–13294. https://doi.org/10.1021/jp101300w.

Mason, S.E., Iceman, C.R., Tanwar, K.S., Trainor, T.P., Chaka, A.M., 2009. Pb(II) adsorption on isostructural hydrated alumina and hematite (0001) surfaces: a DFT study. J. Phys. Chem. C 113 (6), 2159–2170. https://doi.org/10.1021/jp807321e.

Mason, S.E., Trainor, T.P., Chaka, A.M., 2011. Hybridization-reactivity relationship in Pb (II) adsorption on α-Al_2O_3-water interfaces: a DFT study. J. Phys. Chem. C 115 (10), 4008–4021. https://doi.org/10.1021/jp108201f.

Mason, S.E., Corum, K.W., Ramadugu, S.K., 2015. Fundamental insights about environmental interface reactivity from DFT calculations of geochemical model systems. Surf. Sci. 631, 48–56. https://doi.org/10.1016/j.susc.2014.07.033.

Momma, K., Izumi, F., 2011. VESTA 3 for three-dimensional visualization of crystal, volumetric and morphology data. J. Appl. Crystallogr. 44 (6), 1272–1276. https://doi.org/10.1107/S0021889811038970.

Monkhorst, H.J., Pack, J.D., 1976. Special points for Brillouin-zone integrations. Phys. Rev. B 13 (12), 5188–5192. https://doi.org/10.1103/PhysRevB.13.5188.
Murray, H.H., 2000. Traditional and new applications for kaolin, smectite, and palygorskite: a general overview. Appl. Clay Sci. 17 (5), 207–221. https://doi.org/10.1016/S0169-1317(00)00016-8.
Murray, H.H., 2006. Clays. Ullmann's Encyclopedia of Industrial Chemistry. John Wiley & Sons, Weinheim, Germany. https://doi.org/10.1002/14356007.a07_109.pub2.
Nisar, J., Århammar, C., Jämstorp, E., Ahuja, R., 2011. Optical gap and native point defects in kaolinite studied by the GGA-PBE, HSE functional, and GW approaches. Phys. Rev. B 84 (7), 7–15. https://doi.org/10.1103/physrevb.84.075120.
Perdew, J.P., Burke, K., Ernzerhof, M., 1996. Generalized gradient approximation made simple. Phys. Rev. Lett. 77 (18), 3865–3868. https://doi.org/10.1103/PhysRevLett.77.3865.
Richard, D., Rendtorff, N.M., 2019. First principles study of structural properties and electric field gradients in kaolinite. Appl. Clay Sci. 169, 67–73. https://doi.org/10.1016/j.clay.2018.12.013.
Rubasinghege, G., Ogden, S., Baltrusaitis, J., Grassian, V.H., 2013. Heterogeneous uptake and adsorption of gas-phase formic acid on oxide and clay particle surfaces: the roles of surface hydroxyl groups and adsorbed water in formic acid adsorption and the impact of formic acid adsorption on water uptake. J. Phys. Chem. A 117 (44), 11316–11327. https://doi.org/10.1021/jp408169w.
Sato, H., Ono, K., Johnston, C.T., Yamagishi, A., 2004. First-principle study of polytype structures of 1:1 dioctahedral phyllosilicates. Am. Mineral. 89 (11–12), 1581–1585. https://doi.org/10.2138/am-2004-11-1201.
Schroeder, P.A., Erickson, G., 2014. Kaolin: from ancient porcelains to nanocomposites. Elements 10 (3), 177–182. https://doi.org/10.2113/gselements.10.3.177.
Song, K.-H., Wang, X., Qian, P., Zhang, C., Zhang, Q., 2013. Theoretical study of interaction of formamide with kaolinite. Comput. Theor. Chem. 1020, 72–80. https://doi.org/10.1016/j.comptc.2013.07.027.
Sposito, G., 2008. The Chemistry of Soils, 2nd ed. Oxford University Press, New York.
Sposito, G., Skipper, N.T., Sutton, R., Park, S.-H., Soper, A.K., Greathouse, J.A., 1999. Surface geochemistry of the clay minerals. P Natl. Acad. Sci. USA 96 (7), 3358. https://doi.org/10.1073/pnas.96.7.3358.
Tamijani, A.A., Bjorklund, J.L., Augustine, L.J., Catalano, J.G., Mason, S.E., 2020. Density functional theory and thermodynamics modeling of inner-sphere oxyanion adsorption on the hydroxylated α-Al_2O_3(001) surface. Langmuir. https://doi.org/10.1021/acs.langmuir.0c01203.
Torn, L.H., de Keizer, A., Koopal, L.K., Lyklema, J., 2003. Mixed adsorption of poly (vinylpyrrolidone) and sodium dodecylbenzenesulfonate on kaolinite. J. Colloid Interface Sci. 260 (1), 1–8. https://doi.org/10.1016/S0021-9797(03)00046-8.
Tosoni, S., Doll, K., Ugliengo, P., 2006. Hydrogen bond in layered materials: structural and vibrational properties of kaolinite by a periodic B3LYP approach. Chem. Mater. 18 (8), 2135–2143. https://doi.org/10.1021/cm060227e.
Towns, J., Cockerill, T., Dahan, M., Foster, I., Gaither, K., Grimshaw, A., Hazlewood, V., Lathrop, S., Lifka, D., Peterson, G.D., Roskies, R., Scott, J.R., Wilkins-Diehr, N., 2014. XSEDE: accelerating scientific discovery. Comput. Sci. Eng. 16 (5), 62–74. https://doi.org/10.1109/MCSE.2014.80.
Tunega, D., Bučko, T., Zaoui, A., 2012. Assessment of ten DFT methods in predicting structures of sheet silicates: importance of dispersion corrections. J. Chem. Phys. 137 (11), 114105. https://doi.org/10.1063/1.4752196.
Vanderbilt, D., 1990. Soft self-consistent pseudopotentials in a generalized eigenvalue formalism. Phys. Rev. B 41 (11), 7892–7895. https://doi.org/10.1103/PhysRevB.41.7892.
Wang, J., Xia, S., Yu, L., 2015. Adsorption of Pb(II) on the kaolinite(001) surface in aqueous system: a DFT approach. Appl. Surf. Sci. 339, 28–35. https://doi.org/10.1016/j.apsusc.2015.02.114.
Wang, Q., Kong, X.-P., Zhang, B.-H., Wang, J., 2017. Adsorption of Zn(II) on the kaolinite (001) surfaces in aqueous environment: a combined DFT and molecular dynamics study. Appl. Surf. Sci. 414, 405–412. https://doi.org/10.1016/j.apsusc.2017.04.062.
Wang, G., Lai, Y., Peng, C., 2018. Adsorption of rare earth yttrium and ammonium ions on kaolinite surfaces: a DFT study. Theor. Chem. Accounts 137 (4), 53. https://doi.org/10.1007/s00214-018-2230-3.
Weck, P.F., Kim, E., Jové-Colón, C.F., 2015. Relationship between crystal structure and thermo-mechanical properties of kaolinite clay: beyond standard density functional theory. Dalton Trans. 44, 12550–12560. https://doi.org/10.1039/c5dt00590f.
Williams, E.L., Grosjean, D., 1992. Exposure of deacidified and untreated paper to ambient levels of sulfur dioxide and nitrogen dioxide: nature and yields of reaction products. J. Am. Inst. Conserv. 31 (2), 199–212. https://doi.org/10.1179/019713692806066655.
Wu, Z., Cohen, R.E., 2006. More accurate generalized gradient approximation for solids. Phys. Rev. B 73 (23), 235116. https://doi.org/10.1103/PhysRevB.73.235116.
Young, R.A., Hewat, A.W., 1988. Verification of the triclinic crystal structure of kaolinite. Clay Clay Miner. 36 (3), 225–232. https://doi.org/10.1346/CCMN.1988.0360303.
Zachara, J.M., Cowan, C.E., Schmidt, R.L., Ainsworth, C.C., 1988. Chromate adsorption by kaolinite. Clay Clay Miner. 36 (4), 317–326. https://doi.org/10.1346/CCMN.1988.0360405.
Zhang, Z., Fenter, P., Cheng, L., Sturchio, N.C., Bedzyk, M.J., Předota, M., Bandura, A., Kubicki, J.D., Lvov, S.N., Cummings, P.T., Chialvo, A.A., Ridley, M.K., Bénézeth, P., Anovitz, L., Palmer, D.A., Machesky, M.L., Wesolowski, D.J., 2004. Ion adsorption at the rutile–water interface: linking molecular and macroscopic properties. Langmuir 20 (12), 4954–4969. https://doi.org/10.1021/la0353834.
Zhang, Z., Fenter, P., Kelly, S.D., Catalano, J.G., Bandura, A.V., Kubicki, J.D., Sofo, J.O., Wesolowski, D.J., Machesky, M.L., Sturchio, N.C., Bedzyk, M.J., 2006. Structure of hydrated Zn^{2+} at the rutile TiO_2 (110)-aqueous solution interface: comparison of X-ray standing wave, X-ray absorption spectroscopy, and density functional theory results. Geochim. Cosmochim. Acta 70 (16), 4039–4056. https://doi.org/10.1016/j.gca.2006.06.325.
Zhang, R., Yan, W., Jing, C., 2014. Mechanistic study of PFOS adsorption on kaolinite and montmorillonite. Coll. Surf. A 462, 252–258. https://doi.org/10.1016/j.colsurfa.2014.09.019.
Zhao, J., He, M.-C., 2014. Theoretical study of heavy metal Cd, Cu, Hg, and Ni(II) adsorption on the kaolinite(001) surface. Appl. Surf. Sci. 317, 718–723. https://doi.org/10.1016/j.apsusc.2014.08.162.